On the use of evanescent plane waves for low-frequency energy transmission across material interfaces

Daniel C. Woods, J. Stuart Bolton, and Jeffrey F. Rhoads[a)]
School of Mechanical Engineering, Ray W. Herrick Laboratories, and Birck Nanotechnology Center, Purdue University, West Lafayette, Indiana 47907, USA

(Received 3 February 2015; revised 9 June 2015; accepted 13 August 2015; published online 13 October 2015)

The transmission of airborne sound into high-impedance media is of interest in several applications. For example, sonic booms in the atmosphere may impact marine life when incident on the ocean surface, or affect the integrity of existing structures when incident on the ground. Transmission across high impedance-difference interfaces is generally limited by reflection and refraction at the surface, and by the critical angle criterion. However, spatially decaying incident waves, i.e., inhomogeneous or evanescent plane waves, may transmit energy above the critical angle, unlike homogeneous plane waves. The introduction of a decaying component to the incident trace wavenumber creates a nonzero propagating component of the transmitted normal wavenumber, so energy can be transmitted across the interface. A model of evanescent plane waves and their transmission across fluid-fluid and fluid-solid interfaces is developed here. Results are presented for both air-water and air-solid interfaces. The effects of the incident wave parameters (including the frequency, decay rate, and incidence angle) and the interfacial properties are investigated. Conditions for which there is no reflection at the air-solid interface, due to impedance matching between the incident and transmitted waves, are also considered and are found to yield substantial transmission increases over homogeneous incident waves.
[http://dx.doi.org/10.1121/1.4929692]

[ANN] Pages: 2062–2078

I. INTRODUCTION

The transmission of airborne sound into water has been studied extensively, motivated by applications that include the detection of aircraft by underwater sensors,[1,2] the estimation of sediment properties,[3] and concerns regarding the effects of man-made noise on marine life.[4,5] The transmission of acoustic waves from air into solids is also of interest, such as in assessing the ground pressure patterns resulting from sonic booms,[6–8] which may affect the integrity of building structures. Low-frequency sound, in particular, can be transmitted over large distances in air, and thus often constitutes a substantial portion of the total sound that impinges on such surfaces.

Pressure and energy transmission across the air-water and air-solid interfaces are generally limited by the reflection and refraction at the interface, which are attributable to the large differences in the densities and wave speeds in the two media.[9–11] In addition, for homogeneous, or classical, plane waves, it is well documented that no energy can be transmitted into lossless media by components incident above the critical angle, an angle that is typically quite small given the large differences in wave speeds. An incident homogeneous wave above the critical angle yields a decaying pressure field in the material below the interface, but no energy propagates beyond the interface. However, if spatially decaying incident waves are considered, termed inhomogeneous or evanescent plane waves, energy can be transmitted across the interface even above the critical angle of incidence. By introducing a decaying component into the incident trace wavenumber, the wavenumber components of the transmitted wave are composed of both propagating and decaying terms for all oblique angles of incidence. Consequently, the surface normal wavenumber in the second material (i.e., in the medium below the interface) has a nonzero propagating (real) part, and energy thus propagates away from the interface into the second medium. In fact, for the case of the air-solid interface (or, generically, a given fluid-solid interface), values for the angle and decay rate of the incident wave can be found such that no reflected wave is generated at the interface, which is attributable to the exact matching of the incident impedance by the sum of the impedance contributions from the transmitted longitudinal and transverse, or shear, waves. Moreover, in the region near the zero of the reflection coefficient, the energy transmitted across the interface can be increased substantially compared to homogeneous plane waves below the critical angle. The intensity does, however, decay with distance into the second medium due to the spatial decay characteristics of the incident, and transmitted, waves.

In the context of high impedance-difference interfaces, much work has been presented on the air-water interface,[1–5,12–29] due to the significance of the air-ocean interface in naval applications. Significant contributions include those of Urick,[1,2] who investigated underwater sound propagation, including that from aircraft, and Chapman *et al.*,[19,20] who developed a normal mode theory for sound transmission in a homogeneous atmosphere. Subsequent studies have

a)Electronic mail: jfrhoads@purdue.edu

extended the normal mode theory to include effects from moving sources, inhomogeneous atmospheres, stratified seabeds, and other environmental conditions,[3,5,21–29] with most investigations being primarily concerned with aircraft and sonic booms as the sources of airborne noise. Sonic booms have also been studied for the air-ground interface due to the resulting ground pressure patterns.[6–8] For the reverse scenario (i.e., where the source is in a liquid or solid and the waves are transmitted to air), Godin[30–34] and others[35–37] have investigated conditions for anomalous transparency with a low-frequency source close to the interface, owing to the evanescent waves generated at the surface and the lower speed of sound in the air medium (which cannot be exploited when the source is instead situated in air).

Evanescent plane waves can be produced by using phased arrays of sources and the spectral division method,[38–40] or by the transmission of homogeneous waves through selective absorbing geometries,[41] among other methods,[42,43] which allows for arbitrary variation of the decay rate. For example, the decay rate can be tuned in the spectral division method with a rectangular array by varying the amplitudes and phases of the individual sources. The energy flux in the presence of such waves, as well as the phenomena occurring at material interfaces, have been studied both theoretically and experimentally.[41,44–46] Notably, a minimum of the reflection coefficient is observed near the Rayleigh angle for incident inhomogeneous waves in both lossless and dissipative media. The representation of such waves by complex wavevectors is analogous to the representation of waves in dissipative or heterogeneous media,[10,11,47,48] where the imaginary part of each wavevector component corresponds to decay in that direction. This approach is also analogous to the representation of Gaussian beams in high-frequency acoustic and electromagnetic fields.[49–52]

The goal of the present work was to characterize the pressure and intensity transmission across material interfaces for low-frequency, incident evanescent plane waves, including those incident above the critical angle for homogeneous plane waves. To this end, a model of evanescent plane waves and their transmission across fluid-fluid and fluid-solid interfaces was developed. The interface model extends the theory of the interaction of semi-infinite, homogeneous media presented by Brekhovskikh[9] to allow for incident evanescent waves. The present work builds on the initial efforts of Jessop,[53] who studied multi-layer propagation in the context of energetic materials. "Low-frequency" waves were considered here to be in the frequency range up to 1500 Hz, which permits transmission over reasonably large distances in air. Numerical results are presented for the air-water interface and for typical air-solid interfaces. The effects of the parameters of the incident wave (including the frequency, decay rate, and incidence angle) and those of the interface materials (including the density and wave speed ratios) are also investigated. The conditions for zero reflection, and maximal energy transmission, are explored for the air-solid interface by tuning the parameters of the incident wave near the Rayleigh angle. It is hoped that the theoretical investigations presented here provide an initial basis for the use of evanescent waves for increased energy transmission across high impedance-difference material interfaces, including above the critical angle of incidence, for a range of existing and future applications.

II. REPRESENTATION OF EVANESCENT PLANE WAVES

For a harmonic plane wave traveling in a homogeneous, isotropic fluid of constant speed of sound c and away from material interfaces (i.e., in free space), the complex acoustic pressure $\tilde{p}$ can be represented as[11]

$$\tilde{p} = \tilde{A} e^{j(\omega t - \vec{k}\cdot\vec{r})}, \tag{1}$$

where $\tilde{A}$ is the complex amplitude, ω is the angular frequency, t is the time variable, $\vec{k}$ is the propagation vector, and $\vec{r}$ is the position vector. When utilizing a Cartesian coordinate system, the position vector can be expressed in terms of the respective unit vectors: $\vec{r} = x\hat{e}_x + y\hat{e}_y + z\hat{e}_z$. The propagation vector, or wavevector, can likewise be expressed, for an arbitrary direction of propagation, as

$$\vec{k} = k_x\hat{e}_x + k_y\hat{e}_y + k_z\hat{e}_z, \tag{2}$$

where the k_n are the wavevector components in the respective directions. For plane longitudinal waves propagating in a linear, inviscid fluid, the magnitude of the wavevector, and the wavevector components, satisfy the relation[11]

$$|\vec{k}|^2 = k_x^2 + k_y^2 + k_z^2 = \left(\frac{\omega}{c}\right)^2. \tag{3}$$

The scalar quantity $k = |\vec{k}| = \omega/c$ is known as the material wavenumber.

Homogeneous plane waves exhibit a constant pressure amplitude and phase on any plane perpendicular to the propagation direction. That is, in the absence of material dissipation, the pressure does not decay in any dimension for the harmonic wave. Such homogeneous plane waves are thus represented by real components k_n in the wavevector, which together give the direction of propagation.

In contrast, evanescent waves are disturbances that show an exponential decay in one or more dimensions not aligned with the propagation direction. Examples include surface waves, such as Rayleigh, Lamb, and Stoneley waves, as well as bulk evanescent waves.[9,41,45] In general, such inhomogeneous waves may simultaneously decay and propagate in arbitrary directions. Each of the wavevector components is represented as a complex quantity, where the real part represents propagation and the imaginary part represents exponential decay of the wave, in the respective dimensions: $\tilde{k}_x = \alpha_x - j\beta_x$, $\tilde{k}_y = \alpha_y - j\beta_y$, and $\tilde{k}_z = \alpha_z - j\beta_z$. Substitution of the complex components into Eq. (1) yields

$$\tilde{p} = \tilde{A} e^{-\beta_x x - \beta_y y - \beta_z z} e^{j(\omega t - \alpha_x x - \alpha_y y - \alpha_z z)}. \tag{4}$$

Note that the real parts of the wavevector components give the direction of propagation, $\vec{\alpha} = \alpha_x\hat{e}_x + \alpha_y\hat{e}_y + \alpha_z\hat{e}_z$, and the imaginary parts give the direction of decay, $\vec{\beta} = \beta_x\hat{e}_x + \beta_y\hat{e}_y + \beta_z\hat{e}_z$.

In non-dissipative media, evanescent waves decay along a vector perpendicular to the direction of propagation, and the propagation and decay characteristics can be represented by complex angles of propagation. By using this representation, the angles can be integrated directly into the theory for homogeneous waves, including interactions at material interfaces. In the case of two-dimensional propagation, one of the wavevector components is zero, and the wave characteristics can be represented by a single complex angle.

Figure 1 shows a two-dimensional (i.e., $\tilde{k}_y = 0$) plane wave propagating in free space. When using the complex angle $\tilde{\theta} = \theta_r + j\theta_i$ (in radians), the wavevector components $\tilde{k}_x$ and $\tilde{k}_z$ are determined, as for a real angle, by using the sine and cosine functions, i.e.,

$$\begin{aligned}\tilde{k}_x &= k\sin(\theta_r + j\theta_i)\\ &= k\sin(\theta_r)\cosh(\theta_i) + jk\cos(\theta_r)\sinh(\theta_i),\\ \tilde{k}_z &= k\cos(\theta_r + j\theta_i)\\ &= k\cos(\theta_r)\cosh(\theta_i) - jk\sin(\theta_r)\sinh(\theta_i).\end{aligned} \tag{5}$$

In this formulation, the imaginary part of the complex angle prescribes the rate of exponential decay. The wave decays as $e^{-\beta\delta}$, where δ is the position measured perpendicular to the propagation direction, and the decay parameter β is given by

$$\beta = k\sinh(\theta_i). \tag{6}$$

Substitution of Eq. (5) into Eq. (1) yields

$$\tilde{p} = \tilde{A}e^{-\beta[-\cos(\theta_r)x + \sin(\theta_r)z]}e^{j[\omega t - k\sin(\theta_r)\cosh(\theta_i)x - k\cos(\theta_r)\cosh(\theta_i)z]}. \tag{7}$$

The real component θ_r of the complex angle thus gives the physical direction of propagation, and the imaginary part θ_i controls the decay rate and the effect of the decay on phase propagation. Note also that the phase is constant on any plane perpendicular to the propagation direction, but the amplitude is not.

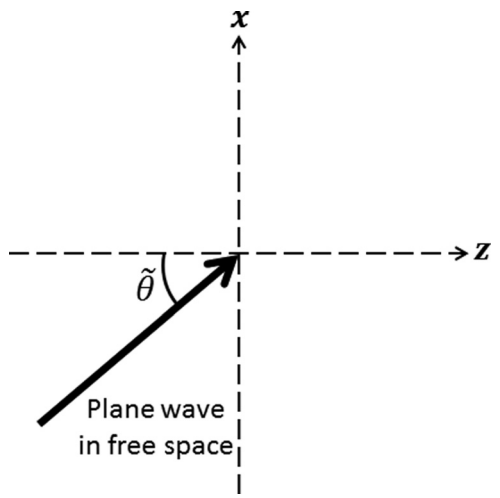

FIG. 1. A diagram of a two-dimensional plane wave propagating in free space.

The sense of decay along the line perpendicular to the propagation direction is determined by the sign of the imaginary part θ_i. If the decay parameter β is prescribed, then the value of θ_i, which represents the corresponding rate of decay can be obtained by inverting Eq. (6), i.e.,

$$\theta_i = \pm\ln\left(\frac{|\beta|}{k} + \left[\left(\frac{\beta}{k}\right)^2 + 1\right]^{1/2}\right), \tag{8}$$

where the sign of θ_i coincides with that of β.

Evanescent plane waves of the type discussed here are spatially distributed disturbances of infinite extent. An analogy can be made with spatially distributed waves that exhibit concentrated peaks in amplitude, such as Gaussian beams. However, in the case of evanescent plane waves, the unidirectional spatial decay characteristics perpendicular to the direction of propagation imply growth without bound in the opposite direction: this is clearly not possible. That being said, like homogeneous plane waves, the representation can be a reasonable approximation over a given region of space, where the pressure phase is approximately constant on any perpendicular plane and where the pressure amplitude varies exponentially.[38,39]

III. EVANESCENT WAVE TRANSMISSION ACROSS MATERIAL INTERFACES

For acoustic waves traveling in air, or in other low-density fluids, energy transmission into liquid or solid media is generally limited by the large impedance difference, which causes significant reflection at the interface.[9–11] In addition, liquid and solid media typically have wave speeds much greater than the speed of sound in air, which causes significant refraction beyond the interface in the liquid or solid medium. It is well known that for incident homogeneous plane waves, no energy can be transmitted across an elastic interface above the critical angle, and an exponentially decaying pressure field is generated in the second medium. In terms of the wavevector, the transmitted wave propagates along ("clings to") the interface, and the normal wavevector component is purely imaginary. Thus, no energy propagates away from the interface and into the second medium.

However, for incident evanescent plane waves which simultaneously propagate and decay, energy can be transmitted at physical angles above the critical angle. Through the introduction of a decaying component in the incident trace wavenumber, the transmitted trace wavenumber (e.g., $\tilde{k}_x$) is given both propagating and decaying components for all oblique incidence angles, which in turn also yields propagating and decaying terms in the transmitted normal wavenumber (e.g., $\tilde{k}_z$) to satisfy Eq. (3). Therefore, the transmitted wave travels at a physical angle below the interface line, with a nonzero real part of the normal wavenumber, and energy can propagate away from the interface into the second material.

Evanescent wave transmission is investigated here for a single material interface, where homogeneous, lossless media occupy the two acoustic half-spaces on either side of

the interface. The incident medium is assumed to be a fluid, and both fluid and solid media are considered for the second medium. Fluid media support longitudinal waves, but cannot sustain shear waves. The fluid media on the incident and transmitted sides of the interface are thus characterized by densities ρ_1 and ρ_2, respectively, and longitudinal wave speeds c_1 and c_2, respectively. In solids, transverse waves can also propagate, and the solid medium is additionally characterized by the shear wave speed b_2. For homogeneous wave incidence, $\theta_{cr} = \arcsin(c_1/c_2)$ gives the critical angle for longitudinal waves and, in the case of the solid medium, $\theta_{cr,s} = \arcsin(c_1/b_2)$ gives the critical angle for shear waves. For small ratios c_1/c_2 and c_1/b_2, the critical angles are close to zero, or normal incidence, which prevents energy transmission for most angles. However, as alluded to in the preceding text, the use of incident evanescent waves effectively eliminates the critical angle criterion.

A. Fluid-fluid interface

A diagram of the fluid-fluid interface is shown in Fig. 2 for two-dimensional propagation in the xz plane, where a right-handed Cartesian coordinate system is assumed. In general, reflected and transmitted longitudinal waves are generated at the interface. The incident wave is assumed to decay perpendicular to the direction of propagation and is represented by the complex angle $\tilde{\theta}_1 = \theta_{1,r} + j\theta_{1,i}$. The reflected angle matches that of the incident wave, and the transmitted angle is denoted as $\tilde{\theta}_2 = \theta_{2,r} + j\theta_{2,i}$. The details of the computation of the transmitted angle, and transmitted wavevector, are given in the Appendix. Both fluid media are considered linear and inviscid, so no shear waves propagate on either side of the interface.

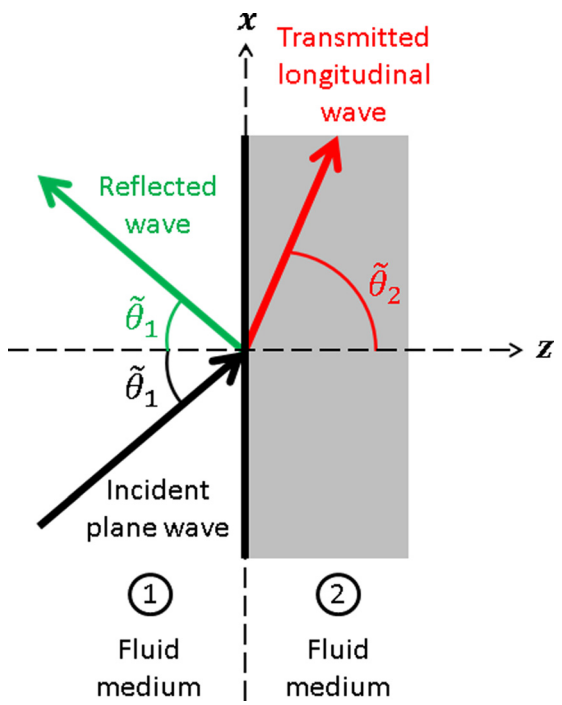

FIG. 2. (Color online) A diagram of the incident, reflected, and transmitted waves at the fluid-fluid interface.

The pressure and particle velocity associated with the transmitted wave can be derived by using the longitudinal wave potentials.[9] The potential on the incident side of the interface is the sum of the potentials associated with the incident and reflected waves

$$\tilde{\phi}_1 = \tilde{\Lambda} e^{j[\omega t - k_1 \sin(\tilde{\theta}_1)x]}\left[e^{-jk_1 \cos(\tilde{\theta}_1)z} + \tilde{V} e^{jk_1 \cos(\tilde{\theta}_1)z}\right], \tag{9}$$

where $\tilde{\Lambda}$ is the potential amplitude of the incident wave, $\tilde{V}$ is the reflection coefficient, and $k_1 = \omega/c_1$ is the material wavenumber in the incident fluid. On the transmitted side, the only disturbance is the transmitted longitudinal wave, the potential of which, using the associated transmission coefficient $\tilde{W}$, is given as

$$\tilde{\phi}_2 = \tilde{\Lambda}\tilde{W} e^{j[\omega t - k_2 \sin(\tilde{\theta}_2)x - k_2 \cos(\tilde{\theta}_2)z]}, \tag{10}$$

where $k_2 = \omega/c_2$ is the material wavenumber of the second fluid.

The boundary conditions at the interface (i.e., at $z = 0$) require continuity of the normal component of the particle velocity and continuity of the normal stress.[9] The velocity vector in either of the media is calculated as the gradient of the wave potential: $\vec{\tilde{u}}_l = \nabla\tilde{\phi}_l$. The normal velocities in the fluids on the incident and transmitted sides of the interface are thus computed as $\tilde{u}_{1,z} = \partial\tilde{\phi}_1/\partial z$ and $\tilde{u}_{2,z} = \partial\tilde{\phi}_2/\partial z$, respectively. Continuity of the trace wavenumber $\tilde{k}_x$ across the interface, also known as generalized Snell's law, follows from the normal velocity condition

$$k_1 \sin(\tilde{\theta}_1) = k_2 \sin(\tilde{\theta}_2). \tag{11}$$

The normal stress rates in the first and second media are given by $\dot{\tilde{\sigma}}_{1,zz} = \rho_1 c_1^2 \nabla^2 \tilde{\phi}_1$ and $\dot{\tilde{\sigma}}_{2,zz} = \rho_2 c_2^2 \nabla^2 \tilde{\phi}_2$, respectively, where the dot denotes the partial derivative with respect to time, $\partial/\partial t$.

The solution of the two boundary conditions at the interface yields the expressions for the coefficients $\tilde{V}$ and $\tilde{W}$ (Ref. 9),

$$\tilde{V} = \frac{\tilde{Z}_2 - \tilde{Z}_1}{\tilde{Z}_2 + \tilde{Z}_1},$$
$$\tilde{W} = \frac{\rho_1}{\rho_2}\left(\frac{2\tilde{Z}_2}{\tilde{Z}_2 + \tilde{Z}_1}\right), \tag{12}$$

where $\tilde{Z}_1 = \rho_1 c_1/\cos(\tilde{\theta}_1)$ and $\tilde{Z}_2 = \rho_2 c_2/\cos(\tilde{\theta}_2)$ are the surface normal impedances for longitudinal waves in the first and second fluids, respectively.

In the first and second media, the pressures are, respectively, $\tilde{p}_1 = -j\omega\rho_1\tilde{\phi}_1$ and $\tilde{p}_2 = -j\omega\rho_2\tilde{\phi}_2$. It can be observed that the pressure amplitude $\tilde{A}$ of the incident wave is related to the amplitude $\tilde{\Lambda}$ of its wave potential by $\tilde{A} = -j\omega\rho_1\tilde{\Lambda}$.

The normal particle velocities on each side of the interface can be calculated directly from the wave potentials by using the expressions given in the preceding text. In the first and second fluids, the normal velocities can be expressed, respectively, as

$$\tilde{u}_{1,z} = \frac{\tilde{A}}{\tilde{Z}_1} e^{j\left[\omega t - k_1 \sin\left(\tilde{\theta}_1\right)x\right]} \left[e^{-jk_1 \cos\left(\tilde{\theta}_1\right)z} - \tilde{V} e^{jk_1 \cos\left(\tilde{\theta}_1\right)z}\right],$$

$$\tilde{u}_{2,z} = \frac{\rho_2}{\rho_1}\left(\frac{\tilde{A}\tilde{W}}{\tilde{Z}_2}\right) e^{j\left[\omega t - k_2 \sin\left(\tilde{\theta}_2\right)x - k_2 \cos\left(\tilde{\theta}_2\right)z\right]}. \quad (13)$$

B. Fluid-solid interface

The analysis presented in Sec. III A is extended here to the case of a solid medium on the transmitted side of the interface. Solid materials support shear stresses, so transmitted shear waves are also generated by the interaction at the interface. Figure 3 shows a diagram of the fluid-solid interface, where a right-handed Cartesian coordinate system is again assumed. The shear wave propagates at the transmitted shear angle, $\tilde{\gamma}_2 = \gamma_{2,r} + j\gamma_{2,i}$, and with the shear wave speed b_2 in the solid medium. The details of the computation of the transmitted shear angle and wavevector are likewise given in the Appendix.

Of particular note for the fluid-solid interface is the phenomena that occur near the Rayleigh angle. Rayleigh waves constitute a particular surface wave solution to the wave equation whereby the longitudinal and shear waves travel at a common velocity along the interface of the solid half-space, which may be bordered by vacuum or, for generalized Rayleigh waves, by an ambient fluid.[9,54,55] If a homogeneous plane wave in the ambient fluid is incident at the elastic interface above the critical angle, a Rayleigh surface wave is generated, the energy of which, in the absence of material dissipation, is reemitted to yield total reflection, and no bulk wave is transmitted. In contrast, if an evanescent plane wave is incident on the solid, bulk evanescent waves (both longitudinal and shear) are transmitted, and the amplitudes are greatest at the Rayleigh angle. A minimum in the reflection coefficient is observed at this angle,[41,45] owing to the resonance phenomenon (and increased transmission) that occurs when the excitation is coincident with the free wave solution. Thus, the use of an incident evanescent wave, in generating the transmitted bulk waves, provides a mechanism for energy to propagate below the interface, which is maximized at the Rayleigh angle.

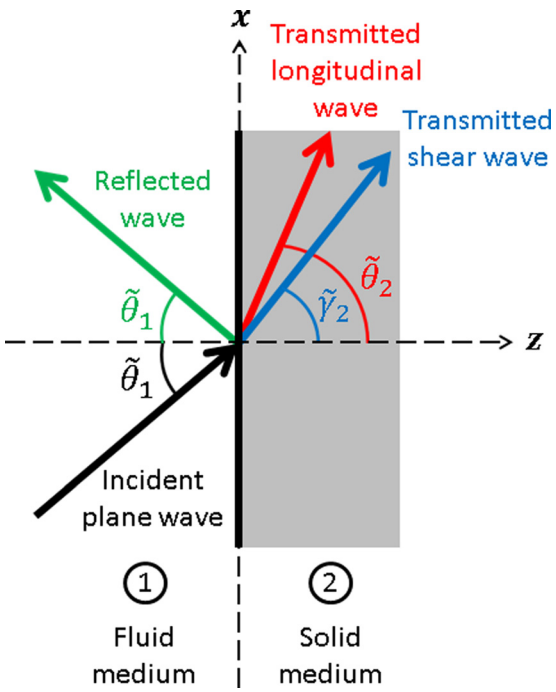

FIG. 3. (Color online) A diagram of the incident, reflected, and transmitted waves at the fluid-solid interface.

The Rayleigh wave speed c_{Ray} for an elastic half-space is computed from the characteristic equation[9,54]

$$\left(\frac{c_{Ray}}{b_2}\right)^6 - 8\left(\frac{c_{Ray}}{b_2}\right)^4 + 8\left[3 - 2\left(\frac{b_2}{c_2}\right)^2\right] \times \left(\frac{c_{Ray}}{b_2}\right)^2 - 16\left[1 - \left(\frac{b_2}{c_2}\right)^2\right] = 0, \quad (14)$$

which has a unique positive real root such that $c_{Ray} < b_2$. The Rayleigh angle can be subsequently computed as $\theta_{Ray} = \arcsin(c_1/c_{Ray})$.

The derivation for the fluid-solid interface parallels that of the fluid-fluid interface except that, in general, transverse waves also exist in the solid medium.[9] The longitudinal potential is as given in Eq. (10), and the shear wave potential is given by

$$\tilde{\psi}_2 = \tilde{\Lambda}\tilde{W}_s\, e^{j\left[\omega t - \kappa_2 \sin\left(\tilde{\gamma}_2\right)x - \kappa_2 \cos\left(\tilde{\gamma}_2\right)z\right]}, \quad (15)$$

where $\tilde{W}_s$ is the transmission coefficient for the shear wave potential and $\kappa_2 = \omega/b_2$ is the material shear wavenumber in the solid material.

The boundary conditions at the interface require, as before, continuity of the normal particle velocity and continuity of the normal stress. In addition, the shear stress must also be continuous across the interface, which necessitates that the shear stress in the solid be zero at the interface, since the incident fluid medium is assumed to be inviscid and thus cannot sustain shear waves.[9] The velocity vector in the solid medium is computed as the sum of the gradient of the longitudinal potential and the curl of the shear potential's associated vector field $\vec{\tilde{\Psi}}_2$: $\vec{\tilde{u}}_2 = \nabla\tilde{\phi}_2 + \nabla \times \vec{\tilde{\Psi}}_2$. For the case of two-dimensional propagation, the shear potential field is simply $\vec{\tilde{\Psi}}_2 = \tilde{\psi}_2\hat{e}_y$, and the normal velocity in the solid reduces to $\tilde{u}_{2,z} = \partial\tilde{\phi}_2/\partial z + \partial\tilde{\psi}_2/\partial x$. Continuity of the trace wavenumber, which also includes the shear trace wavenumber $\tilde{\kappa}_{2,x} = \kappa_2 \sin(\tilde{\gamma}_2)$, again follows from the normal velocity condition

$$k_1 \sin(\tilde{\theta}_1) = k_2 \sin(\tilde{\theta}_2) = \kappa_2 \sin(\tilde{\gamma}_2). \quad (16)$$

The normal stress rate in the solid medium also includes contributions from the shear wave potential and is given as[9]

$$\dot{\tilde{\sigma}}_{2,zz} = \rho_2 c_2^2 \nabla^2\tilde{\phi}_2 + 2\rho_2 b_2^2\left(\frac{\partial^2\tilde{\psi}_2}{\partial x \partial z} - \frac{\partial^2\tilde{\phi}_2}{\partial x^2}\right). \quad (17)$$

Similarly, the shear stress rate in the solid, which must be zero at the interface, is expressed as[9]

$$\dot{\tilde{\sigma}}_{2,xz} = \rho_2 b_2^2\left(2\frac{\partial^2\tilde{\phi}_2}{\partial x \partial z} + \frac{\partial^2\tilde{\psi}_2}{\partial x^2} - \frac{\partial^2\tilde{\psi}_2}{\partial z^2}\right). \quad (18)$$

Solving for the three boundary conditions at the interface yields the expressions for the coefficients $\tilde{V}$, $\tilde{W}$, and $\tilde{W}_s$. Brekhovskikh[9] gives the solution in terms of the transmitted shear angle $\tilde{\gamma}_2$,

$$\tilde{V} = \frac{\tilde{Z}_2 \cos^2(2\tilde{\gamma}_2) + \tilde{Z}_{2,s} \sin^2(2\tilde{\gamma}_2) - \tilde{Z}_1}{\tilde{Z}_2 \cos^2(2\tilde{\gamma}_2) + \tilde{Z}_{2,s} \sin^2(2\tilde{\gamma}_2) + \tilde{Z}_1},$$

$$\tilde{W} = \frac{\rho_1}{\rho_2}\left[\frac{2\tilde{Z}_2 \cos(2\tilde{\gamma}_2)}{\tilde{Z}_2 \cos^2(2\tilde{\gamma}_2) + \tilde{Z}_{2,s} \sin^2(2\tilde{\gamma}_2) + \tilde{Z}_1}\right],$$

$$\tilde{W}_s = \frac{\rho_1}{\rho_2}\left[\frac{2\tilde{Z}_{2,s} \sin(2\tilde{\gamma}_2)}{\tilde{Z}_2 \cos^2(2\tilde{\gamma}_2) + \tilde{Z}_{2,s} \sin^2(2\tilde{\gamma}_2) + \tilde{Z}_1}\right], \quad (19)$$

where $\tilde{Z}_{2,s} = \rho_2 b_2 / \cos(\tilde{\gamma}_2)$ is the surface normal impedance for shear waves in the solid medium.

The pressure in the incident fluid is again given by $\tilde{p}_1 = -j\omega\rho_1\tilde{\phi}_1$. In the solid, each stress component can be computed by dividing the corresponding stress rate by $j\omega$. The transmitted normal and shear stresses can be expanded and written, respectively, in terms of the pressure amplitude $\tilde{A}$ of the incident wave as

$$\tilde{\sigma}_{2,zz} = \frac{\rho_2\tilde{A}}{\rho_1}\left\{\tilde{W}\left[2\left(\frac{b_2}{c_2}\right)^2 \sin^2(\tilde{\theta}_2) - 1\right] \times e^{j[\omega t - k_2 \sin(\tilde{\theta}_2)x - k_2 \cos(\tilde{\theta}_2)z]} - \tilde{W}_s \sin(2\tilde{\gamma}_2) e^{j[\omega t - \kappa_2 \sin(\tilde{\gamma}_2)x - \kappa_2 \cos(\tilde{\gamma}_2)z]}\right\},$$

$$\tilde{\sigma}_{2,xz} = \frac{\rho_2\tilde{A}}{\rho_1}\left\{\tilde{W}_s \cos(2\tilde{\gamma}_2) e^{j[\omega t - \kappa_2 \sin(\tilde{\gamma}_2)x - \kappa_2 \cos(\tilde{\gamma}_2)z]} - \tilde{W}\left(\frac{b_2}{c_2}\right)^2 \sin(2\tilde{\theta}_2) e^{j[\omega t - k_2 \sin(\tilde{\theta}_2)x - k_2 \cos(\tilde{\theta}_2)z]}\right\}. \quad (20)$$

Finally, the particle velocities in the solid medium can be computed from the wave potentials using the expression given in the preceding text. For the normal and tangential components of the velocity, this yields, respectively,

$$\tilde{u}_{2,z} = \frac{\rho_2\tilde{A}}{\rho_1}\left\{\frac{\tilde{W}}{\tilde{Z}_2} e^{j[\omega t - k_2 \sin(\tilde{\theta}_2)x - k_2 \cos(\tilde{\theta}_2)z]} + \frac{\tilde{W}_s \sin(\tilde{\gamma}_2)}{\rho_2 b_2} e^{j[\omega t - \kappa_2 \sin(\tilde{\gamma}_2)x - \kappa_2 \cos(\tilde{\gamma}_2)z]}\right\},$$

$$\tilde{u}_{2,x} = \frac{\rho_2\tilde{A}}{\rho_1}\left\{\frac{\tilde{W} \sin(\tilde{\theta}_2)}{\rho_2 c_2} e^{j[\omega t - k_2 \sin(\tilde{\theta}_2)x - k_2 \cos(\tilde{\theta}_2)z]} - \frac{\tilde{W}_s}{\tilde{Z}_{2,s}} e^{j[\omega t - \kappa_2 \sin(\tilde{\gamma}_2)x - \kappa_2 \cos(\tilde{\gamma}_2)z]}\right\}. \quad (21)$$

C. Intensity transmission

The instantaneous intensity of an acoustic wave is the rate of energy transmission per unit area in the direction of propagation.[10,11] For harmonic waves, the instantaneous intensity can be time-averaged to give the acoustic intensity. The intensity is represented as a vector $\vec{I}$, where the components correspond to the acoustic intensities in the respective directions. For stress tensor $\tilde{\sigma}_{mn}$ and velocity vector $\tilde{u}_m$, the components of the instantaneous energy flux vector (per unit area) in lossless media are expressed as[44,45,56]

$$E_n(t) = -\sum_{m=1}^{3} \Re(\tilde{\sigma}_{mn})\Re(\tilde{u}_m), \quad (22)$$

where $\Re$ denotes the real part of the argument and the subscripts 1–3 correspond to the x, y, and z directions, respectively. The intensity is computed by time-averaging the energy flux over one period

$$I_n = \frac{\omega}{2\pi}\int_{t_0}^{t_0+2\pi/\omega} E_n(\tau)\mathrm{d}\tau, \quad (23)$$

where t_0 is an arbitrary time.

An inviscid fluid cannot support shear stresses, so by using the pressure ($\tilde{p} = -\tilde{\sigma}_{xx} = -\tilde{\sigma}_{zz}$), the tangential and normal intensities can be computed conveniently as $I_x = \Re(\tilde{p}\tilde{u}_x^*)/2$ and $I_z = \Re(\tilde{p}\tilde{u}_z^*)/2$, where the asterisk denotes the complex conjugate. In the solid, however, these expressions cannot be used, as the contributions of the shear stresses to the energy flux must be taken into account.[44,56] The longitudinal and transverse waves propagate with different wavenumbers along the respective dimensions and the phase difference must be incorporated by time-averaging according to Eq. (23), where the instantaneous intensities are $E_x = -[\Re(\tilde{\sigma}_{xx})\Re(\tilde{u}_x) + \Re(\tilde{\sigma}_{xz})\Re(\tilde{u}_z)]$ and $E_z = -[\Re(\tilde{\sigma}_{zz})\Re(\tilde{u}_z) + \Re(\tilde{\sigma}_{xz})\,\Re(\tilde{u}_x)]$.

For the incident evanescent waves under consideration, the transmitted normal wavenumbers (i.e., $\tilde{k}_{2,z}$ and, in the case of the solid, $\tilde{\kappa}_{2,z}$) have both propagating and decaying components, corresponding to their real and imaginary parts, respectively. Energy thus propagates away from the interface and into the second material. In terms of the normal intensity expression, the normal particle velocity is related to the wave pressure by the normal wavenumber. When the real part is taken in computing the intensity, the real (propagating) component of the normal wavenumber yields nonzero intensity transmission across the material interface. Conversely, for the case of homogeneous waves incident beyond the critical angle, the transmitted normal wavenumber is purely imaginary and no energy is transmitted; all of the energy is reflected back into the incident medium.

D. Energy conservation in the system

If energy is to be conserved, the energy fluxes approaching and leaving the interface, which are given by the normal intensities I_z in the two media taken at $z = 0$, must balance. Since the boundary conditions at the interface require continuity of the normal particle velocity and continuity of the stress tensor, it can be readily observed from Eq. (22) that the normal intensities are equal at $z = 0$, and energy is conserved at the interface.

Moreover, energy conservation in the media in the presence of the evanescent disturbances can also be demonstrated. It can be shown that, in the absence of material dissipation, there is no net energy flux through any closed control surface S, which may be constructed in either medium or which may stretch across the interface, since the energy flux is continuous through the interface plane.[44,45] (The uppercase S used to denote the control surface should not be confused with the lowercase s used in subscripts to denote quantities associated with shear waves.) The net energy flux through the closed surface is thus given by the surface integral

$$\oiint_S \vec{I}_l \cdot \mathrm{d}\vec{S} = 0, \tag{24}$$

where $\mathrm{d}\vec{S}$ is the differential area element on the control surface, oriented along the outward normal vector to the surface, and l denotes the appropriate medium for the given differential element of S. For the case of two-dimensional propagation in the xz plane, there is no variation in the y direction, and the control surface can be replaced by a closed curve C in the xz plane. (The uppercase C used to denote the closed curve should not be confused with the lowercase c used to denote longitudinal wave speeds.) The surface integral is therefore replaced by a line integral to give the net energy flux per unit width

$$\oint_C \vec{I}_l \cdot \mathrm{d}\vec{C} = 0, \tag{25}$$

where $\mathrm{d}\vec{C}$ is the differential line element of the curve, oriented along the outward normal vector.

IV. RESULTS AND DISCUSSION

The transmitted intensities were investigated for the air-water interface and for various parameters that characterize typical air-solid interfaces. For the air-water interface, the pressure and normal particle velocity distributions in the water medium were also considered. For the air-solid interfaces, the normal stress distributions in the solid were considered, along with the normal particle velocity and intensity distributions. In the case of the solid media, conditions for zero reflection at the interface, and consequently total transmission of the incident normal intensity, were additionally explored.

A. Air-water interface

Methods of energy transmission from the incident air medium into water may be of interest in numerous applications, but are limited for homogeneous plane waves by the critical angle criterion. Considered here is the case of air at 20 °C and 1 atm ($\rho_1 = 1.21$ kg/m^3, $c_1 = 343$ m/s), and fresh water under the same conditions ($\rho_2 = 998$ kg/m^3, $c_2 = 1481$ m/s).[11] The critical angle for the interface is $\theta_{cr} \approx 13.4°$. The incident evanescent plane wave is given a pressure amplitude of $\tilde{A} = 1$ Pa and a frequency of $f = 1000$ Hz ($f = \omega/2\pi$). The transmitted (and incident) pressures and velocities scale with the incident pressure magnitude $|\tilde{A}|$, and the intensities scale with $|\tilde{A}|^2$.

The transmitted normal intensity at the interface (i.e., at $z = 0$) and at the tangential position $x = 0$ was first considered as a function of the incidence angle component $\theta_{1,r}$, which gives the physical angle of propagation according to Eq. (7). Figure 4 shows the transmitted normal intensity (at $x = z = 0$) as a function of the angle $\theta_{1,r}$ for several values of the decay parameter: $\beta = 0$, 0.001, 0.01, and 0.02 rad/m, where the case of a homogeneous plane wave ($\beta = 0$) is included to allow for direct comparison. It should be noted that the intensities of the evanescent waves vary with x and z according to the equations highlighted in the preceding text. Below the critical angle, the evanescent wave intensities are close to those of homogeneous plane waves at the same incidence angles, with little variation with β. Above the critical angle, however, the intensity transmission from evanescent waves remains nonzero and increases with β, although larger values of β also yield more rapid decay with distance into the second medium. The transmitted intensities monotonically decrease with increasing incidence angles beyond the critical angle.

Energy conservation in the second medium is verified here by using an arbitrary sample control volume. Since there is no variation in the y direction, a closed curve C was constructed and the net energy fluxes were given per unit width. The sample curve utilized here took the form of a rectangle in the xz plane, stretching from $x = 0.5$ to 1.5 m and from $z = 0$ to 0.25 m, as shown in Fig. 5. By using Eq. (25), the intensity vector in the second medium $\vec{I}_2(x, z)$, and the unit vectors along the respective coordinate axes ($\hat{e}_x$ and $\hat{e}_z$), the net energy fluxes in units of W/m entering and leaving the planar region ($\dot{Q}_I$ and $\dot{Q}_{II}$, respectively) are given, with the sign convention, as

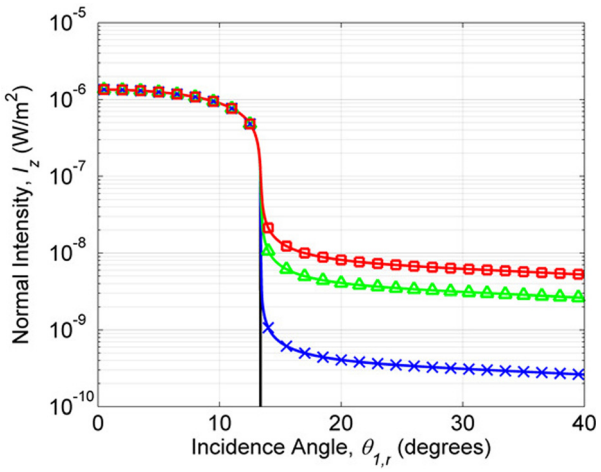

FIG. 4. (Color online) The transmitted normal intensity, at the interface and at tangential position $x = 0$, as a function of the incidence angle for the air-water interface. The markers as ×'s, triangles, and squares on the curves correspond to values of the decay parameter of 0.001, 0.01, and 0.02 rad/m, respectively. The unmarked curve corresponds to a homogeneous plane wave (i.e., no decay). Note that a logarithmic scale has been used for the vertical axis.

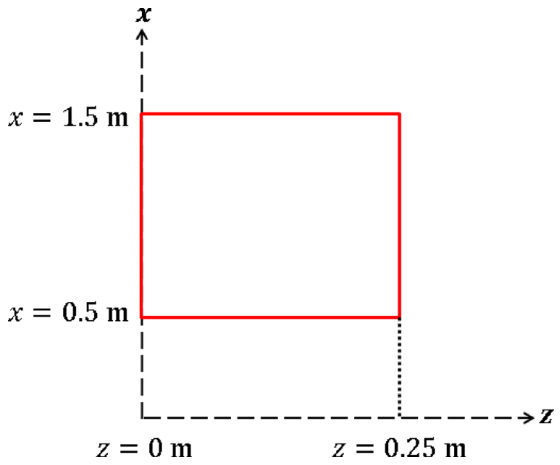

FIG. 5. (Color online) A sample closed curve constructed in the xz plane in the second medium.

$$\begin{aligned}\dot{Q}_I &= \int_0^{0.25} \vec{I}_2(0.5,z)\cdot\hat{e}_x\,\mathrm{d}z + \int_{0.5}^{1.5} \vec{I}_2(x,0)\cdot\hat{e}_z\,\mathrm{d}x \\ &= \int_0^{0.25} I_{2,x}(0.5,z)\,\mathrm{d}z + \int_{0.5}^{1.5} I_{2,z}(x,0)\,\mathrm{d}x, \\ \dot{Q}_{II} &= \int_0^{0.25} \vec{I}_2(1.5,z)\cdot\hat{e}_x\,\mathrm{d}z + \int_{0.5}^{1.5} \vec{I}_2(x,0.25)\cdot\hat{e}_z\,\mathrm{d}x \\ &= \int_0^{0.25} I_{2,x}(1.5,z)\,\mathrm{d}z + \int_{0.5}^{1.5} I_{2,z}(x,0.25)\,\mathrm{d}x, \end{aligned} \tag{26}$$

where the position values are given in m. The results of the computation are presented in Fig. 6 as a function of the incidence angle, with the decay parameter set at a nominal value of $\beta = 0.01$ rad/m. It can be readily observed that the energy flux entering the volume matches the flux exiting the volume, so energy conservation is verified.

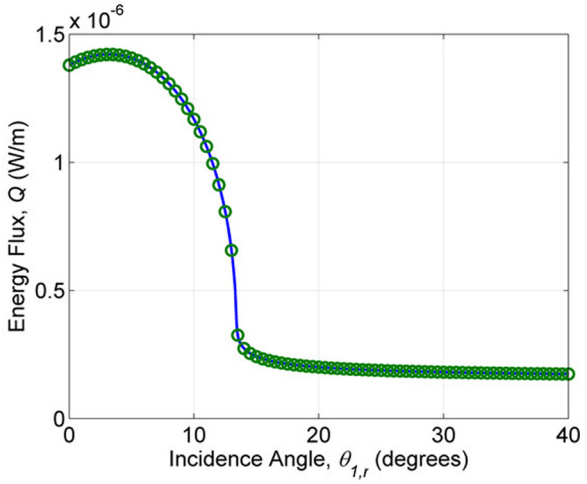

FIG. 6. (Color online) The net energy flux per unit width entering and leaving the sample control volume in water. The solid line and the markers as circles represent the net energy fluxes entering and leaving the volume, respectively. For visual clarity, the energy flux leaving the volume is shown with data points only at 0.5° increments.

The transmitted pressure, normal particle velocity, and normal intensity distributions were also investigated for subcritical and supercritical angles, with the decay parameter set at the nominal value of $\beta = 0.01$ rad/m. Figure 7 gives the pressure, velocity, and intensity distributions in the second medium (water) at a subcritical angle of

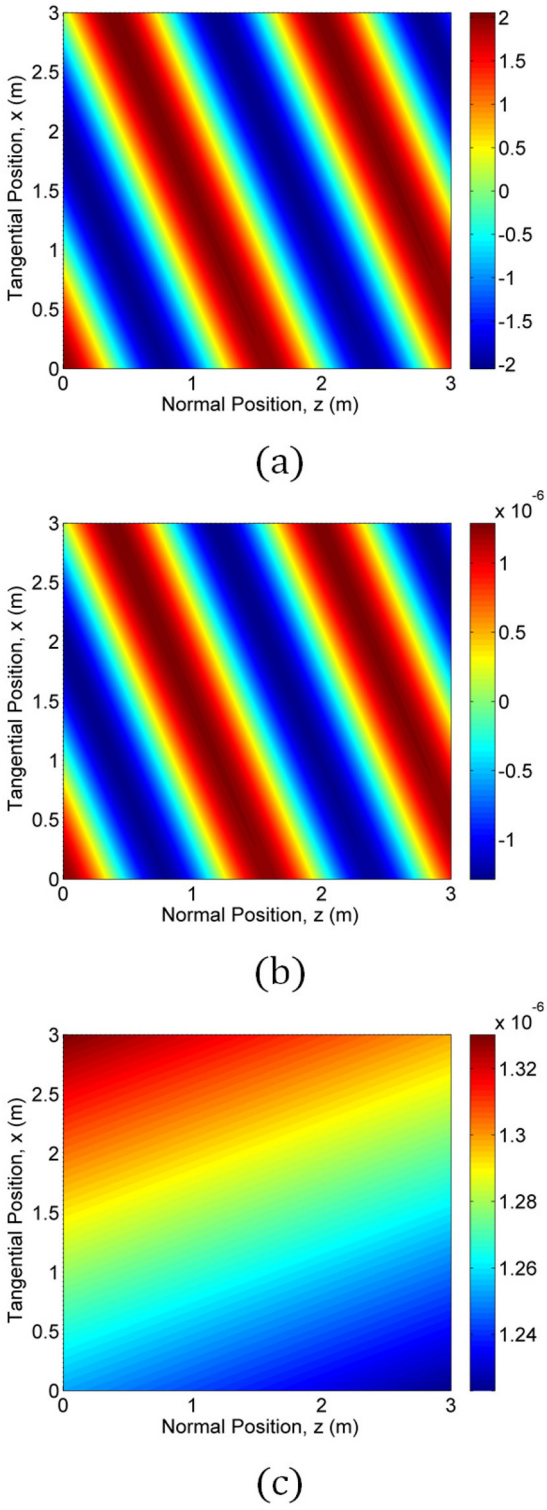

FIG. 7. (Color online) The subcritical transmitted distributions of (a) pressure (in Pa), (b) normal velocity (in m/s), and (c) normal intensity (in W/m^2) for the air-water interface. The subcritical angle is 5° and the decay parameter is 0.01 rad/m.

$\theta_{1,r} = 5°$. The transmitted pressure wave propagates at an angle of approximately 22.1°. It can be observed that the normal particle velocity distribution is similar to that of the pressure, with a small phase difference introduced by the decay of the incident wave. The spatial dependence of the incident wave intensity can be conceptualized as lines of constant intensity along the direction of propagation that are refracted at the interface to yield the transmitted intensity distribution shown in Fig. 7(c). The normal intensity of the transmitted wave is thus constant along the direction of propagation but decays perpendicular to that direction. It should be noted that the spatial decay of the intensity, like the decay of the incident wave pressure, is a characteristic of the disturbance itself and that no dissipation is included in the second medium. At a given tangential position x, the intensity decays with distance into the second material, and the rate of decay is relatively small for the large area shown.

The transmitted pressure, normal velocity, and normal intensity distributions are presented in Fig. 8 for the supercritical angle $\theta_{1,r} = 15°$. The decay parameter was again set at $\beta = 0.01$ rad/m. In this case, the transmitted wave propagates at an angle of approximately 89.7°. The angle is close to, but slightly less than, 90° (i.e., along the interface), so nonzero energy transmission occurs above the critical angle. The pressure and velocity distributions are out of phase with each other, and show the transmitted wave propagating at the slight angle with respect to the interface plane. The amplitudes peak at the interface and decay along a vector nearly aligned with the normal distance into the second medium. The refracted lines of constant intensity again lie along the direction of propagation, and as a result are slightly offset from the interface, as shown in Fig. 8(c). Note that the angle of propagation, although still barely evident as deviating from the tangential axis, is exaggerated in the intensity plot since the horizontal position range is narrower than that of the vertical position. Like the pressure and velocity, the normal intensity distribution decays approximately normal to the interface but, since the pressure and velocity are out-of-phase, it does not show the same spatial variation near the interface. The intensity transmission for most supercritical angles is considerably less than that for the subcritical angles, but remains finite.

B. Air-solid interface

Energy transmission from air into solid materials is also of interest. The incident air medium is again taken at 20 °C and 1 atm ($\rho_1 = 1.21$ kg/m^3, $c_1 = 343$ m/s). Solid materials typically have densities at least 1000 times that of air, and longitudinal wave speeds at least 10 times the speed of sound in air. The density and longitudinal wave speed in the solid medium were thus set at $\rho_2 = 1210$ kg/m^3 ($\rho_2/\rho_1 = 1000$) and $c_2 = 3430$ m/s ($c_2/c_1 = 10$), respectively. The shear wave speed in the solid was taken as $b_2 = 2400$ m/s ($b_2/c_1 = 7$). The critical angles for the interface are $\theta_{cr} \approx 5.7°$ for transmitted longitudinal waves and $\theta_{cr,s} \approx 8.2°$ for transmitted shear waves. The incident wave was again given a pressure amplitude of $\tilde{A} = 1$ Pa and a frequency of $f = 1000$ Hz.

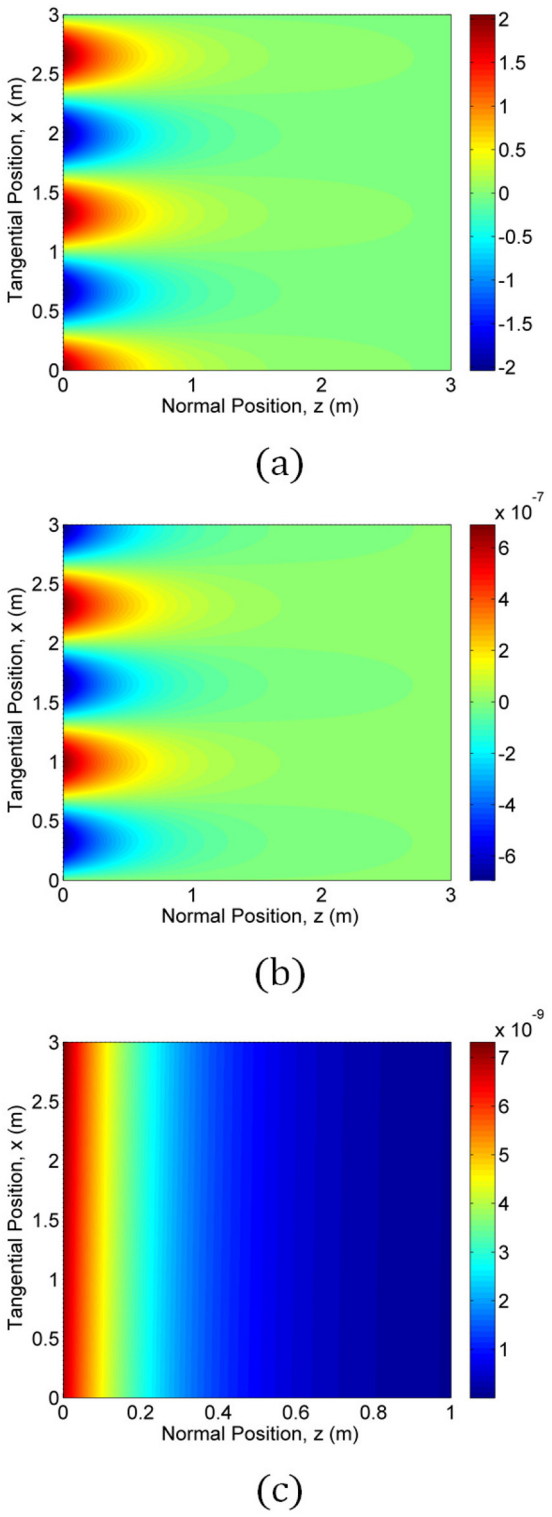

FIG. 8. (Color online) The supercritical transmitted distributions of (a) pressure (in Pa), (b) normal velocity (in m/s), and (c) normal intensity (in W/m^2) for the air-water interface. The supercritical angle is 15° and the decay parameter is 0.01 rad/m. Note that the horizontal axis on the intensity plot shows the decay over only the first 1 m away from the interface.

As for the air-water interface, the transmitted normal intensity, taken at the interface (i.e., at $z = 0$) and at the tangential position $x = 0$, was investigated as a function of the

incidence angle component $\theta_{1,r}$. The normal intensity is shown in Fig. 9 for decay parameter values of $\beta = 0$, 0.001, 0.01, and 0.02 rad/m, where the case of a homogeneous plane wave ($\beta = 0$) is again included for comparison. The evanescent wave intensities are again close to those of homogeneous plane waves for incidence below the critical angles, with negligible variation with β. Between the critical angles, $\theta_{cr} \approx 5.7^\circ$ and $\theta_{cr,s} \approx 8.2^\circ$, the intensities remain close to those of homogeneous plane waves, since the transmitted transverse waves dominate in this regime. However, whereas the transmission from homogeneous waves goes to zero above the critical angle for transverse waves, the intensities from evanescent waves drop significantly slightly above that angle before climbing to a peak near 9.4°, which is the Rayleigh angle as predicted by the wave speed in Eq. (14). At this angle, the incident wave is coincident with the resonance phenomenon of coupled longitudinal and shear waves in the solid half-space. This condition corresponds to a minimum in the reflection coefficient and consequently maximum intensity transmission, which is discussed in depth in Sec. D. Above the supercritical peak, the transmitted intensities monotonically decrease with further increasing incidence angles.

Energy conservation in the solid medium is verified here, again by using the sample control volume shown in Fig. 5. The intensity vector in the solid $\vec{I}_2(x,z)$ is computed with Eq. (23), and the net energy fluxes entering and leaving the planar region are again given by Eq. (26). The results of the computation are given in Fig. 10 as a function of the incidence angle, where the decay parameter is set at $\beta = 0.01$ rad/m. A large increase in energy flux is observed at the Rayleigh angle, attributable to the minimum in the reflection coefficient and the increased intensity transmission. As with the fluid medium considered in the preceding text, it can be readily observed that the energy flux entering the control volume matches the flux exiting, so energy conservation in the solid is verified as well.

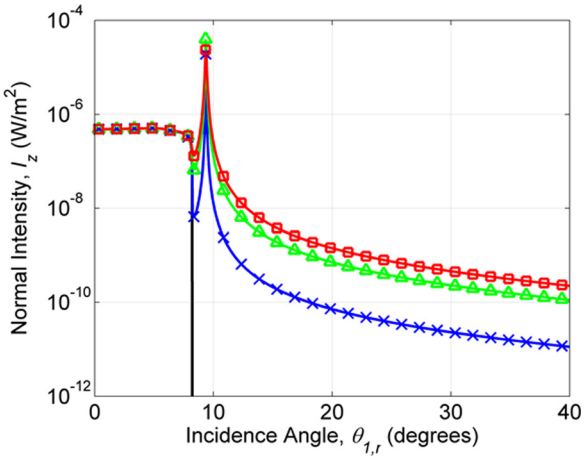

FIG. 9. (Color online) The transmitted normal intensity, at the interface and at tangential position $x = 0$, as a function of the incidence angle for the air-solid interface. The markers as ×'s, triangles, and squares on the curves correspond to values of the decay parameter of 0.001, 0.01, and 0.02 rad/m, respectively. The unmarked curve corresponds to a homogeneous plane wave (i.e., no decay). Note that a logarithmic scale has been used for the vertical axis.

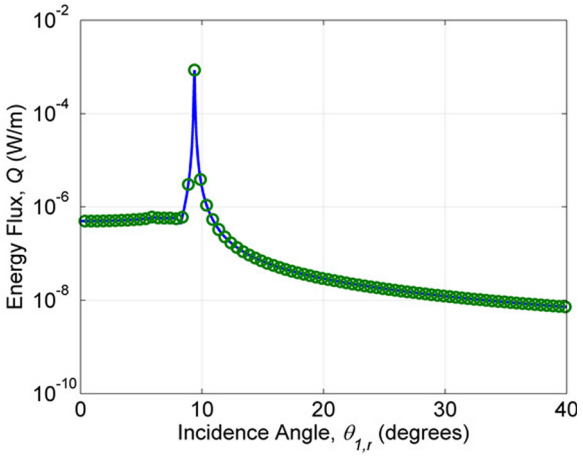

FIG. 10. (Color online) The net energy flux per unit width entering and leaving the sample control volume in the solid. The solid line and the markers as circles represent the net energy fluxes entering and leaving the volume, respectively. For visual clarity, the energy flux leaving the volume is shown with data points only at 0.5° increments. Note that a logarithmic scale has been used for the vertical axis.

Figure 11 depicts the transmitted normal stress, normal particle velocity, and normal intensity distributions for a supercritical angle of $\theta_{1,r} = 15^\circ$ with a decay parameter of $\beta = 0.01$ rad/m. The transmitted longitudinal wave propagates at an angle of approximately 89.87°, and the transmitted shear wave propagates at approximately 89.86°, each less than 90°, thus permitting energy transmission into the solid medium. The transmitted shear angle is always less than the transmitted longitudinal angle, provided the longitudinal wave speed in the solid is greater than the shear wave speed, and both angles asymptotically approach 90° as the incidence angle is increased toward grazing. Due to the interaction of the transmitted longitudinal and shear waves, the transmitted normal stress peaks at a small distance (i.e., a fraction of a wavelength) beneath the interface surface. As with the air-water interface, the normal velocity is out-of-phase with the stress, which is evident in the intensity distribution. The lines of constant intensity in the incident wave can again be conceptualized as refracted in the second medium, but due to the contributions from the transmitted shear wave, the interaction in the solid is more complex. The intensity, however, likewise decays with distance into the second medium, at a slight angle with respect to the interface plane, with the angle again exaggerated in Fig. 11(c) since the horizontal position range is narrower than the vertical range. Also as with the air-water case, no dissipation was incorporated in the solid medium and the spatial decay of the normal intensity is solely a consequence of using incident waves with spatially dependent pressure amplitudes.

C. Effects of frequency, decay rate, and material properties

The effects of the frequency, incident wave decay rate, and density and wave speed ratios for the air-solid interface were considered as well. For these investigations, the incident wave in air ($\rho_1 = 1.21$ kg/m^3, $c_1 = 343$ m/s) was again given a pressure amplitude of $\tilde{A} = 1$ Pa. In addition, except

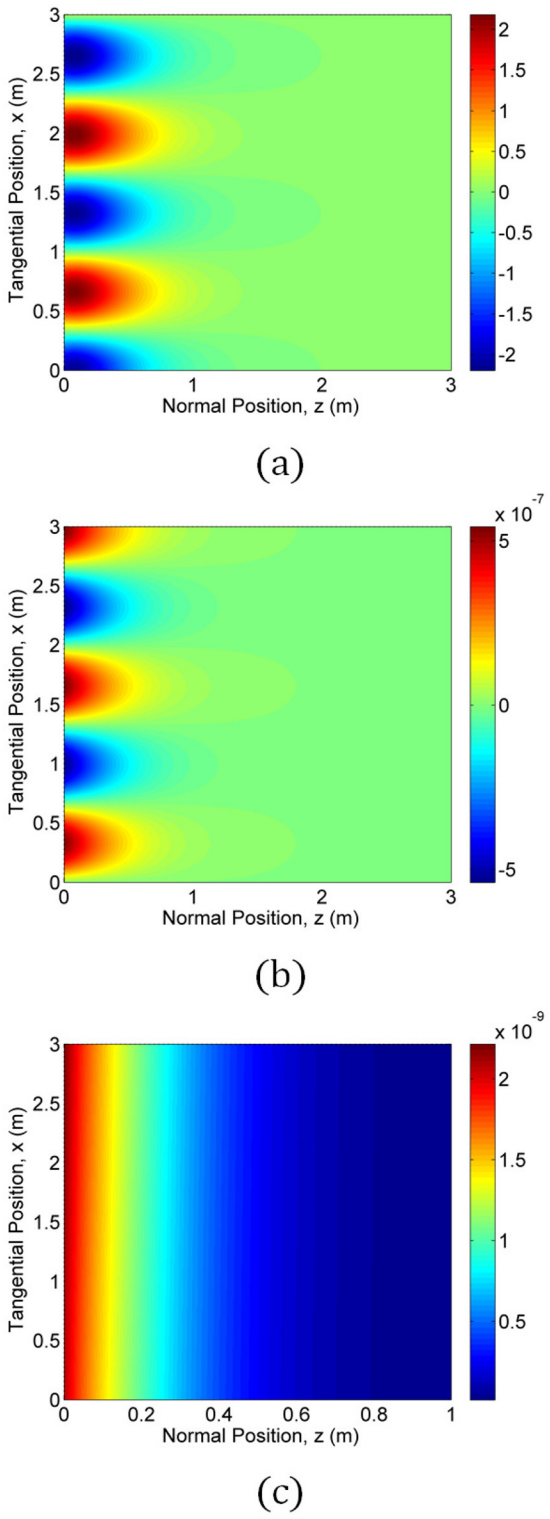

FIG. 11. (Color online) The transmitted distributions of (a) normal stress (in Pa), (b) normal velocity (in m/s), and (c) normal intensity (in W/m^2) for the air-solid interface at a supercritical angle of 15°. The decay parameter is set to 0.01 rad/m. Note that the horizontal axis on the intensity plot shows the decay over only the first 1 m away from the interface.

where the parameters are varied, the nominal values are taken as follows: frequency $f = 1000$ Hz, decay parameter $\beta = 0.01$ rad/m, density ratio $\rho_2/\rho_1 = 1000$, longitudinal wave speed ratio $c_2/c_1 = 10$, and shear wave speed ratio $b_2/c_1 = 7$. For each parameter, three values of the incidence angle were used: $\theta_{1,r} = 5°$, 15°, and 30°. For all cases, the transmitted normal intensity is presented at the interface (i.e., at $z = 0$) and at the tangential position $x = 0$.

The frequency was varied in the range from $f = 100$ to 1500 Hz. The normal intensity as a function of frequency is presented in Fig. 12(a). For the subcritical angle of 5°, the frequency has a negligible effect on the intensity at the interface, with only a slight decrease with increasing frequency, attributable to the decaying component of the incident evanescent wave. However, for all angles, the frequency significantly impacts the spatial variation in the second medium (with shorter variations and more rapid decay observed at higher frequencies), and affects the incident wave potential amplitude $\tilde{\Lambda}$, according to its relation with the pressure amplitude ($\tilde{A} = -j\omega\rho_1\tilde{\Lambda}$). For the supercritical angles, the normal intensities can be observed to monotonically decrease with increasing frequencies and to also decrease for increasing incidence angles.

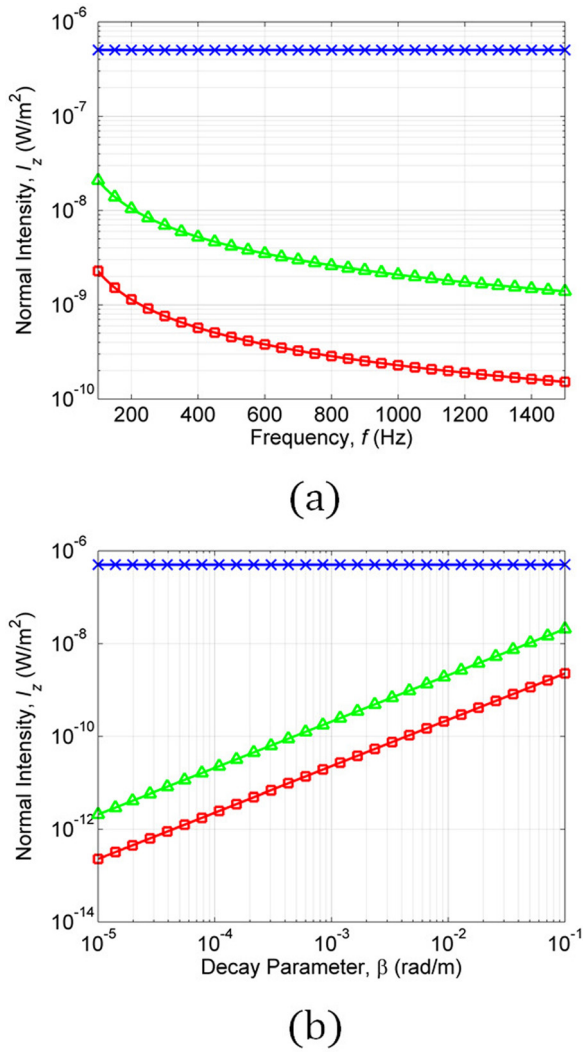

FIG. 12. (Color online) The transmitted normal intensity, at the interface and at tangential position $x = 0$, as a function of (a) frequency and (b) decay parameter. The markers as exes, triangles, and squares on the curves correspond to values of the incidence angle of 5°, 15°, and 30°, respectively. Note that a logarithmic scale has been used for the vertical axes and for the horizontal axis in (b).

To explore the effect of the decay rate, the decay parameter was chosen to remain small and was varied in the range of $\beta = 10^{-5}$ to 10^{-1} rad/m. The normal intensity as a function of the decay parameter is given in Fig. 12(b). In a similar way to the frequency, the decay rate has a negligible impact on the intensity at the interface for the subcritical angle, with slight increases for increasing decay rates. At supercritical angles, a larger effect is evident, with dramatic increases in intensity with increasing decay rates, and with intensities again lower for larger incidence angles. However, when increasing the decay rate of the incident wave, the transmitted waves will decay at a greater rate with distance into the second medium. The transmitted energy is thus increasingly concentrated near the surface for increasing decay rates.

Finally, the effects of the density and wave speed ratios of the interface materials were investigated. The density ratio was varied from $\rho_2/\rho_1 = 10$ to 10^4 to represent a range of typical solid materials, including some high-density solids. Steel and lead, for example, have density ratios of around 6400 and 9300, respectively.[11] By similar considerations, the longitudinal wave speed ratio was varied from $c_2/c_1 = 10$ to 20, and the shear wave speed ratio from $b_2/c_1 = 5$ to 10, to not exceed the longitudinal ratio. The normal intensities as functions of the density ratio, longitudinal wave speed ratio, and shear wave speed ratio are presented in Figs. 13(a), 13(b), and 13(c), respectively. As the density ratio is increased, the difference in the surface normal impedances of the two media also increases, and therefore, more of the intensity is reflected back into the incident medium and less is transmitted. As such, the transmitted normal intensity decreases with increasing density ratio, which is evident in Fig. 13(a). Similarly, increasing the longitudinal wave speed ratio yields greater reflection of the incident intensity, and also greater refraction of the transmitted longitudinal waves, which can be observed for the supercritical angles in Fig. 13(b). In the case of the $\theta_{1,r} = 5^\circ$ curve in Fig. 13(b), the incidence angle is initially subcritical at $c_2/c_1 = 10$, but as the wave speed ratio is increased, the angle becomes coincident with the longitudinal critical angle at $c_2/c_1 \approx 11.4$ (which corresponds to the local decrease in the curve). Above that value, the angle becomes supercritical for longitudinal waves but remains subcritical for transverse waves. Consequently, above the coincident value, shear waves dominate in the second medium and the normal intensity increases with further increasing longitudinal wave speed ratios. With respect to the shear wave speed ratio effect in Fig. 13(c), the variation in the normal intensity is due to the change in the longitudinal wave–shear wave interaction with changes in the shear ratio. The variation for the subcritical angle mirrors that of the supercritical angles, but on a much larger scale. Note that the supercritical angles remain supercritical for both longitudinal and shear waves for all of the shear wave speed values shown. The peaks that are evident for the supercritical angles are due to the minima in the reflection coefficient for the respective incidence angles. The minimum in the reflection coefficient is discussed in Sec. IV D.

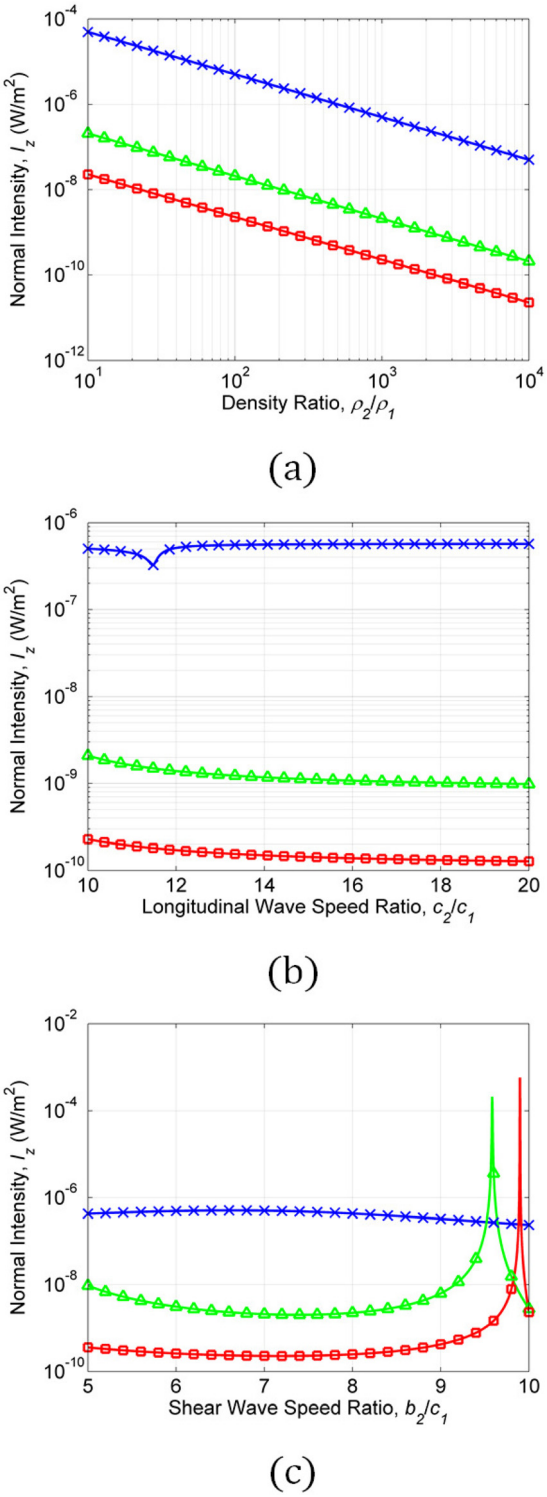

FIG. 13. (Color online) The transmitted normal intensity, at the interface and at tangential position $x = 0$, as a function of (a) density ratio, (b) longitudinal wave speed ratio, and (c) shear wave speed ratio. The markers as exes, triangles, and squares on the curves correspond to values of the incidence angle of 5°, 15°, and 30°, respectively. Note that a logarithmic scale has been used for the vertical axes and for the horizontal axis in (a).

D. Conditions for zero reflection

In the case of the fluid-solid interface, for a prescribed value of the incident wave decay rate, a minimum in the reflection coefficient can be located at a supercritical angle of incidence. The minimum corresponds to the resonance

phenomenon of the coupled longitudinal and shear motions in the solid half-space, which occurs at the Rayleigh angle.[41,45] In terms of the impedances, the local minimum is the point at which the surface normal impedance of the incident wave is closely matched by the sum of the impedance contributions from the transmitted longitudinal and shear waves, and, as such, the effect is not observed for the fluid-fluid interface. In fact, for the fluid-solid interface, the decay rate and incidence angle can be varied to locate a set of values for which the reflection coefficient goes to zero (i.e., exact matching of the incident impedance), which depend on the material properties that characterize the two media. The corresponding decay rate and incidence angle values consequently yield total transmission of the incident normal intensity, since none of the incident energy is reflected.

This phenomenon is shown here for the example of the air-solid interface considered previously. The properties of air are again specified as density $\rho_1 = 1.21\,\mathrm{kg/m^3}$ and longitudinal wave speed $c_1 = 343$ m/s. The properties of the solid medium are likewise again set as density $\rho_2 = 1210\ \mathrm{kg/m^3}$ ($\rho_2/\rho_1 = 1000$), longitudinal wave speed $c_2 = 3430$ m/s ($c_2/c_1 = 10$), and shear wave speed $b_2 = 2400$ m/s ($b_2/c_1 = 7$). As before, the pressure amplitude of the incident wave is $\tilde{A} = 1$ Pa and the frequency is $f = 1000$ Hz.

The location of the zero in the reflection coefficient $\tilde{V}$ was found numerically through variation of the decay parameter β and the incidence angle $\theta_{1,r}$. The values at which the zero occurs are, approximately: $\beta^\star \approx 1.07 \times 10^{-4}$ rad/m and $\theta^\star_{1,r} \approx 9.3657^\circ$. The value of the incidence angle is in agreement with the Rayleigh angle, as predicted by Eq. (14). The topology of the magnitude of the reflection coefficient in the immediate locale of the zero point is shown in Fig. 14. It can be observed that the magnitude increases steeply away from the local minimum, as the ranges shown of the input parameters are narrow. However, the reduction of the reflection coefficient across much wider ranges of the angle and decay rate yields significant increases in the intensity transmission in those wider domains, as is evidenced by the region near the peaks in Fig. 9. Note that, in Fig. 9, dramatic increases in the intensity are observed even for decay rates that far exceed the value of $\beta^\star$. In addition, sources creating a band of incidence angles and decay rate components may

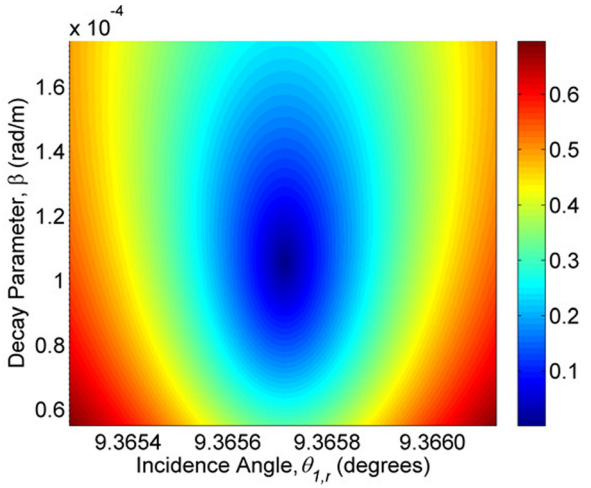

FIG. 14. (Color online) The magnitude of the reflection coefficient near the zero point as a function of the incidence angle and decay parameter for the air-solid interface.

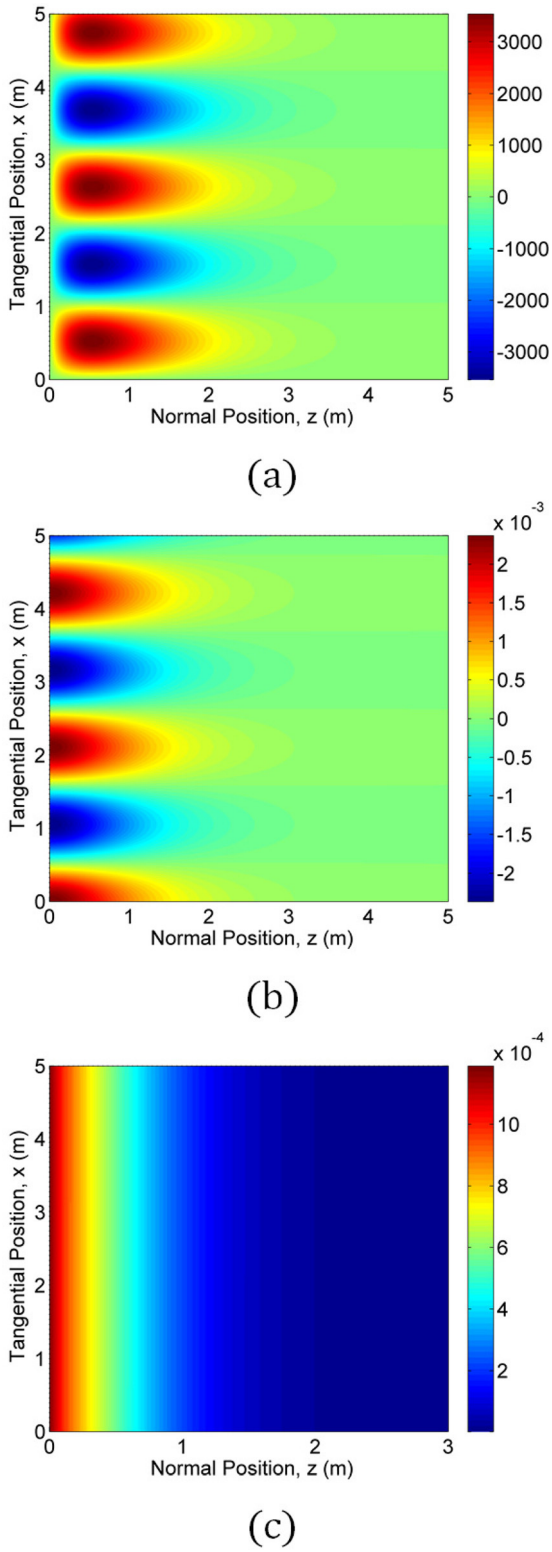

FIG. 15. (Color online) The transmitted distributions of (a) normal stress (in Pa), (b) normal velocity (in m/s), and (c) normal intensity (in $\mathrm{W/m^2}$) near the reflection coefficient zero point for the air-solid interface. Note that the horizontal axis on the intensity plot shows the decay over only the first 3 m away from the interface.

be used in practice to exploit the phenomenon around the zero point for increased energy transmission.

Much greater values of the transmitted normal stress, as well as the normal intensity, can be achieved for incidence angles and decay rates near the zero of the reflection coefficient. With reference to Eq. (19), at the minimum, the impedance contributions from the transmitted longitudinal and shear waves cancel that of the incident wave to yield a zero in the numerator of $\tilde{V}$. Consequently, the denominator of the transmission coefficients (excluding the density ratio) is $2\tilde{Z}_1$, and the transmitted normal stress terms in Eq. (20) are proportional to $\tilde{Z}_2/\tilde{Z}_1$ and $\tilde{Z}_{2,s}/\tilde{Z}_1$, which are large ratios for the high impedance difference (note that the density ratio in the coefficient equations cancels with that in the stress equation, and enters in the coefficient equations as a consequence of converting the stress to the wave potential). The transmitted normal stress, normal particle velocity, and normal intensity distributions are presented in Fig. 15 for those parameters corresponding to the approximate zero point. In addition to the much greater amplitudes, the peak in the transmitted stress is shifted a greater distance beneath the interface surface for the case of zero reflection. The transmitted normal intensity near the interface is on the order of 10^{-3} W/m^2, more than 1500 times that transmitted at subcritical angles by homogeneous waves. The zero point corresponds to total intensity transmission, as no reflected wave is generated. Values of the decay rate and incidence angle away from the zero point, as expected, yield less intensity transmission. But, again referring to the peaks observed in Fig. 9, compared to homogeneous waves, the intensity transmission is increased dramatically across reasonable ranges of the input parameters. In the case of the incident evanescent waves, however, the intensity decays normal to the surface at a rate which increases with the decay parameter β.

V. CONCLUSIONS

A model for the transmission of low-frequency, evanescent plane waves across fluid-fluid and fluid-solid material interfaces has been presented. For both interfaces, nonzero energy transmission was shown to occur for all oblique angles of incidence, owing to the introduction of a decaying component in the incident wave, which yields a nonzero propagating (real) part of the transmitted normal wavenumber even above the critical angle. Numerical results were presented that demonstrate the phenomena for the air-water interface and for typical air-solid interfaces. The transmitted intensities decay with distance into the media below the interface, attributable to the spatial decay characteristics of the incident and transmitted waves, but the intensities remain nonzero for all such angles of incidence. The rate of decay in the second medium depends on the frequency, angle, and decay rate of the incident wave as well as on the interface material properties. For the fluid-solid interface, an incidence angle and decay rate could be found for which the reflection coefficient is zero and intensity transmission is maximized, to yield energy transmission on the order of 1500 times that from homogeneous waves at subcritical incidence. This phenomenon at the Rayleigh angle is attributable to the spatial resonance that occurs when the excitation is coincident with the coupled free wave solution, and the transmitted bulk evanescent waves provide a mechanism for energy propagation beyond the material interface.

Potential applications of the air-water interface results include extensions or improvements to existing efforts, such as the detection of aircraft using underwater sensors.[1,2] Energy transmission decreases with increasing incidence angles, particularly above the critical angle, but remains finite to allow for a wide range of incidence angle components. The subsurface peak in the transmitted stress for the air-solid interface, which is due to the interaction of the transmitted longitudinal and shear waves, may prove useful in a number of applications, for example, in medical applications that could include subsurface ablation,[57–59] diagnostics of pulmonary conditions,[60] and sound therapy in bone healing.[61,62] Similarly, the zero in the reflection coefficient for the air-solid interface may be utilized in applications that seek to maximize energy transmission, as it yields substantial increases over classical, homogeneous waves. As noted, this phenomenon can be exploited for significant transmission increases not only at the zero point, but also in the surrounding neighborhood of incidence angles and decay rates. Applications under development may also make use of the large transmission distances of low-frequency waves for stand-off energy transmission above the critical angle. For instance, in the context of trace vapor detection of hidden explosives, it has been suggested that low-frequency stand-off acoustic excitation, which can penetrate metal barriers, may be able to heat target energetic materials to increase vapor pressures and so facilitate detection.[63–67]

Future work will attempt to extend the results included here to finite media, which is of particular interest for media with dimensions on the order of (or smaller than) an acoustic wavelength, and also account for dissipation and inhomogeneities in the materials. The work will also consider the use of finite, spatially distributed waves, such as Gaussian beams.[49–52] In addition, sound field reproduction techniques, including those analogous to methods for classical plane waves and random pressure fields,[68–71] will be further explored for evanescent waves. This work will continue the investigation of methods of energy transmission across high impedance-difference interfaces through theory and experimentation.

ACKNOWLEDGMENTS

This research is supported by the U.S. Office of Naval Research through a Multidisciplinary University Research Initiative on Sound and Electromagnetic Interacting Waves under ONR Grant No. N00014-10-1-0958. The authors are also grateful to the reviewers for their helpful comments.

APPENDIX: CALCULATION OF TRANSMITTED WAVEVECTORS

For two-dimensional propagation in the xz plane, the transmitted wavevector can be computed using the condition for trace wavenumber continuity, $\tilde{k}_{1,x} = \tilde{k}_{2,x}$, and the

condition for the material wavenumber, Eq. (3). The transmitted trace wavenumber $\tilde{k}_{2,x}$ is simply that of the incident wave. By using the material wavenumber of the second medium k_2 and Eq. (3), the transmitted normal wavenumber is

$$\tilde{k}_{2,z} = \pm(k_2^2 - \tilde{k}_{2,x}^2)^{1/2}, \tag{A1}$$

where the sign should be chosen to yield a negative imaginary part, which represents decay with distance into the second medium.

In the case of the solid medium on the transmission side of the interface, the shear wavevector must also be computed. Again using the condition for trace wavenumber continuity, the transmitted shear trace wavenumber $\tilde{\kappa}_{2,x}$ is also that of the incident wave: $\tilde{\kappa}_{2,x} = \tilde{k}_{1,x}$. And with the material shear wavenumber κ_2, the transmitted shear normal component can likewise be computed as

$$\tilde{\kappa}_{2,z} = \pm(\kappa_2^2 - \tilde{\kappa}_{2,x}^2)^{1/2}, \tag{A2}$$

with the sign again chosen to yield a negative imaginary part.

For evanescent waves that decay along the line perpendicular to the direction of propagation, the transmitted angles can be computed directly, which can in turn be used to calculate the normal wavenumbers: $\tilde{k}_{2,z} = k_2\cos(\tilde{\theta}_2)$ and, for the solid, $\tilde{\kappa}_{2,z} = \kappa_2\cos(\tilde{\gamma}_2)$. By writing the material wavenumbers in the trace wavenumber continuity equation, Eq. (16), in terms of the frequency and wave speeds, the frequency dependence in the relation can be eliminated. Also, by expanding the sine terms, as in Eq. (5), and equating the real and imaginary parts, one obtains

$$\begin{aligned}\sin(\theta_{2,r}) &= \frac{c_2}{c_1}\left[\frac{\cosh(\theta_{1,i})}{\cosh(\theta_{2,i})}\right]\sin(\theta_{1,r}),\\ \cos(\theta_{2,r}) &= \frac{c_2}{c_1}\left[\frac{\sinh(\theta_{1,i})}{\sinh(\theta_{2,i})}\right]\cos(\theta_{1,r}).\end{aligned} \tag{A3}$$

It is assumed here that the real part $\theta_{1,r}$ of the incidence angle is positive and, thus, the imaginary part $\theta_{1,i}$ must also be positive to yield decay into the second medium. If the real part $\theta_{1,r}$ were negative, then $\theta_{1,i}$ would also be negative. In that case, the negative root in the transmitted angle component $\theta_{2,i}$ would be chosen as the physical solution, again to yield decay with distance into the second material: but otherwise the computations are the same as those presented here.

The real part $\theta_{2,r}$ of the transmitted angle satisfies the trigonometric identity

$$\sin^2(\theta_{2,r}) + \cos^2(\theta_{2,r}) = 1, \tag{A4}$$

and the substitution of the expressions from Eq. (A3) yields

$$\begin{aligned}&\left[\frac{\cosh(\theta_{1,i})}{\cosh(\theta_{2,i})}\right]^2\sin^2(\theta_{1,r}) + \left[\frac{\sinh(\theta_{1,i})}{\sinh(\theta_{2,i})}\right]^2\cos^2(\theta_{1,r})\\ &\quad= \left(\frac{c_1}{c_2}\right)^2.\end{aligned} \tag{A5}$$

Since the incidence angle $\tilde{\theta}_1 = \theta_{1,r} + j\theta_{1,i}$ is known, $\theta_{2,i}$ is the only unknown quantity in Eq. (A5). The equation can be solved for any values of the wave speed ratio and incidence angle. Note first that the solution for $\theta_{2,i}$ must be real, owing to the expanded form of the transmitted angle, $\tilde{\theta}_2 = \theta_{2,r} + j\theta_{2,i}$. At $\theta_{2,i} = 0$, the value of the left-hand side of Eq. (A5) is infinite. As $\theta_{2,i}$ is increased from zero, the values of $\cosh(\theta_{2,i})$ and $\sinh(\theta_{2,i})$ increase monotonically, so the left-hand side decreases monotonically. Therefore, $\theta_{2,i}$ can be increased until the value of the left-hand side matches the finite, positive value of the right-hand side, $(c_1/c_2)^2$, to yield the unique solution $\theta_{2,i}^{\star}$. The equation has even symmetry in $\theta_{2,i}$, as each term in Eq. (A5) is squared. However, the physical solution is the positive root in $\theta_{2,i}$, which yields decay of the wave with distance into the second medium. Equation (A5) can thus be solved numerically for the unique positive real root to yield the solution $\theta_{2,i}^{\star}$, which was the approach taken here. [Note, however, that Eq. (A5) can alternatively be expressed in terms of exponentials by using the definitions of the hyperbolic functions. The resulting equation is eighth-order in $\theta_{2,i}$, with even symmetry, which can be solved in closed form to yield up to eight distinct roots, of which the physical solution is the unique positive real root.]

To solve for the real part of the transmitted angle $\theta_{2,r}$, either of the expressions in Eq. (A3) can be inverted. By using the sine expression, the solution $\theta_{2,r}^{\star}$ is given by

$$\theta_{2,r}^{\star} = \arcsin\left[\frac{c_2\cosh(\theta_{1,i})\sin(\theta_{1,r})}{c_1\cosh(\theta_{2,i}^{\star})}\right]. \tag{A6}$$

For the solid medium, the transmitted shear angle, $\tilde{\gamma}_2 = \gamma_{2,r} + j\gamma_{2,i}$, can be computed by the same method. The quantities $\theta_{2,r}$, $\theta_{2,i}$, and c_2 should be replaced by $\gamma_{2,r}$, $\gamma_{2,i}$, and b_2, respectively, in Eqs. (A3)–(A6).

[1]R. J. Urick, "Noise signature of an aircraft in level flight over a hydrophone in the sea," J. Acoust. Soc. Am. **52**(3), 993–999 (1972).
[2]R. J. Urick, *Principles of Underwater Sound* (McGraw-Hill, New York, 1983), 423 pp.
[3]M. J. Buckingham, E. M. Giddens, F. Simonet, and T. R. Hahn, "Propeller noise from a light aircraft for low-frequency measurements of the speed of sound in a marine sediment," J. Comput. Acoust. **10**(4), 445–464 (2002).
[4]W. J. Richardson, C. R. Greene, Jr., C. I. Malme, and D. H. Thomson, *Marine Mammals and Noise* (Academic, San Diego, CA, 1995), 576 pp.
[5]V. W. Sparrow, "Review and status of sonic boom penetration into the ocean," J. Acoust. Soc. Am. **111**(1), 537–543 (2002).
[6]D. L. Lansing and D. J. Maglieri, "Comparison of measured and calculated sonic-boom ground patterns due to several different aircraft maneuvers," Technical Report No. NASA-TN-D-2730, NASA Langley Research Center, Hampton, VA, 1965.
[7]D. J. Maglieri, D. A. Hilton, and N. J. McLeod, "Experiments on the effects of atmospheric refraction and airplane accelerations on sonic-boom ground-pressure patterns," Technical Report No. NASA-TN-D-3520, NASA Langley Research Center, Hampton, VA, 1966.
[8]M. Downing, N. Zamot, C. Moss, D. Morin, E. Wolski, S. Chung, K. Plotkin, and D. Maglieri, "Controlled focused sonic booms from maneuvering aircraft," J. Acoust. Soc. Am. **104**(1), 112–121 (1998).
[9]L. M. Brekhovskikh, *Waves in Layered Media* (Academic, New York, 1960), 561 pp.
[10]P. M. Morse and K. U. Ingard, *Theoretical Acoustics* (McGraw-Hill, New York, 1968), 927 pp.
[11]L. E. Kinsler, A. R. Frey, A. B. Coppens, and J. V. Sanders, *Fundamentals of Acoustics* (Wiley and Sons, Hoboken, NJ, 1999), 548 pp.

[12]E. Gerjuoy, "Refraction of waves from a point source into a medium of higher velocity," Phys. Rev. **73**(12), 1442–1449 (1948).
[13]A. A. Hudimac, "Ray theory solution for the sound intensity in water due to a point source above it," J. Acoust. Soc. Am. **29**(8), 916–917 (1957).
[14]M. S. Weinstein and A. G. Henney, "Wave solution for air-to-water sound transmission," J. Acoust. Soc. Am. **37**(5), 899–901 (1965).
[15]R. W. Young, "Sound pressure in water from source in air," J. Acoust. Soc. Am. **50**(5), 1392–1393 (1971).
[16]R. W. Young, "Sound pressure in water from a source in air and vice versa," J. Acoust. Soc. Am. **53**(6), 1708–1716 (1973).
[17]W. C. Meecham, "High-frequency model for sound transmission from an airborne source into the ocean," J. Acoust. Soc. Am. **60**(2), 339–342 (1976).
[18]S. C. Lubard and P. M. Hurdle, "Experimental investigation of acoustic transmission from air into a rough ocean," J. Acoust. Soc. Am. **60**(5), 1048–1052 (1976).
[19]D. M. F. Chapman and P. D. Ward, "The normal-mode theory of air-to-water sound transmission in the ocean," J. Acoust. Soc. Am. **87**(2), 601–618 (1990).
[20]D. M. F. Chapman, D. J. Thomson, and D. D. Ellis, "Modeling air-to-water sound transmission using standard numerical codes of underwater acoustics," J. Acoust. Soc. Am. **91**(4), 1904–1910 (1992).
[21]V. S. Buldyrev and N. S. Grigor'eva, "Sound field generated in a water layer of variable depth by a source moving in the atmosphere. I: Time-dependent normal modes," Acoust. Phys. **39**(5) 413–418 (1993).
[22]V. S. Buldyrev and N. S. Grigor'eva, "Sound field generated in a water layer of variable depth by a source moving in the atmosphere. II: Time variation of the normal-mode characteristics," Acoust. Phys. **39**(6), 537–542 (1993).
[23]L. Kazandjian and L. Leviandier, "A normal mode theory of air-to-water sound transmission by a moving source," J. Acoust. Soc. Am. **96**(3), 1732–1740 (1994).
[24]B. G. Ferguson and K. W. Lo, "Transiting aircraft parameter estimation using underwater acoustic sensor data," IEEE J. Ocean. Eng. **24**(4), 424–435 (1999).
[25]R. A. Sohn, F. Vernon, J. A. Hildebrand, and S. C. Webb, "Field measurements of sonic boom penetration into the ocean," J. Acoust. Soc. Am. **107**(6), 3073–3083 (2000).
[26]N. N. Komissarova, "Sound field features in the coastal zone of a shallow sea with an airborne source of excitation," Acoust. Phys. **47**(3), 313–322 (2001).
[27]Z. Y. Zhang, "Modelling of sound transmission from air into shallow and deep waters," in *Proceedings of the Australian Acoustical Society Conference*, Adelaide, Australia (2002), pp. 234–243.
[28]F. Desharnais and D. M. F. Chapman, "Underwater measurements and modeling of a sonic boom," J. Acoust. Soc. Am. **111**(1), 544–553 (2002).
[29]H. K. Cheng and C. J. Lee, "Sonic-boom noise penetration under a wavy ocean: Theory," J. Fluid Mech. **514**, 281–312 (2004).
[30]O. A. Godin, "Anomalous transparency of the water-air interface for low-frequency sound," J. Acoust. Soc. Am. **119**(5), 3253 (2006).
[31]O. A. Godin, "Transmission of low-frequency sound through the water-to-air interface," Acoust. Phys. **53**(3), 305–312 (2007).
[32]O. A. Godin, "Low-frequency sound transmission through a gas–liquid interface," J. Acoust. Soc. Am. **123**(4), 1866–1879 (2008).
[33]O. A. Godin, "Sound transmission through water–air interfaces: New insights into an old problem," Contemp. Phys. **49**(2), 105–123 (2008).
[34]O. A. Godin, "Low-frequency sound transmission through a gas–solid interface," J. Acoust. Soc. Am. **129**(2), EL45–EL51 (2011).
[35]B. E. McDonald and D. C. Calvo, "Enhanced sound transmission from water to air at low frequencies," J. Acoust. Soc. Am. **122**(6), 3159–3161 (2007).
[36]D. C. Calvo, M. Nicholas, and G. J. Orris, "Experimental verification of enhanced sound transmission from water to air at low frequencies," J. Acoust. Soc. Am. **134**(5), 3403–3408 (2013).
[37]A. P. Voloshchenko and S. P. Tarasov, "Effect of anomalous transparency of a liquid-gas interface for sound waves," Acoust. Phys. **59**(2), 163–169 (2013).
[38]D. Trivett, L. Luker, S. Petrie, A. Van Buren, and J. Blue, "A planar array for the generation of evanescent waves," J. Acoust. Soc. Am. **87**(6), 2535–2540 (1990).
[39]H. Itou, K. Furuya, and Y. Haneda, "Evanescent wave reproduction using linear array of loudspeakers," in *Proceedings of the IEEE Workshop on Applications of Signal Processing to Audio and Acoustics*, New Paltz, NY (2011), pp. 37–40.
[40]J. Ahrens, M. R. Thomas, and I. Tashev, "Efficient implementation of the spectral division method for arbitrary virtual sound fields," in *Proceedings of the IEEE Workshop on Applications of Signal Processing to Audio and Acoustics*, New Paltz, NY (2013), pp. 1–4.
[41]M. Deschamps, "Reflection and refraction of the evanescent plane wave on plane interfaces," J. Acoust. Soc. Am. **96**(5), 2841–2848 (1994).
[42]T. J. Matula and P. L. Marston, "Electromagnetic acoustic wave transducer for the generation of acoustic evanescent waves on membranes and optical and capacitor wave-number selective detectors," J. Acoust. Soc. Am. **93**(4), 2221–2227 (1993).
[43]A. Fujii, N. Wakatsuki, and K. Mizutani, "A planar acoustic transducer for near field acoustic communication using evanescent wave," Jpn. J. Appl. Phys. **53**(7), 07KB07 (2014).
[44]M. Hayes, "Energy flux for trains of inhomogeneous plane waves," Proc. R. Soc. Lond. Ser. A Math. Phys. Sci. **370**(1742), 417–429 (1980).
[45]O. Leroy, G. Quentin, and J. Claeys, "Energy conservation for inhomogeneous plane waves," J. Acoust. Soc. Am. **84**(1), 374–378 (1988).
[46]Y. I. Bobrovnitskii, "On the energy flow in evanescent waves," J. Sound Vib. **152**(1), 175–176 (1992).
[47]J. F. Allard and M. Henry, "Fluid–fluid interface and equivalent impedance plane," Wave Motion **43**(3), 232–240 (2006).
[48]J. F. Allard, O. Dazel, J. Descheemaeker, N. Geebelen, L. Boeckx, and W. Lauriks, "Rayleigh waves in air saturated axisymmetrical soft porous media," J. Appl. Phys. **106**(1), 014906 (2009).
[49]M. M. Popov, "A new method of computation of wave fields using Gaussian beams," Wave Motion **4**(1), 85–97 (1982).
[50]L. B. Felsen, "Geometrical theory of diffraction, evanescent waves, complex rays and Gaussian beams," Geophys. J. Int. **79**(1), 77–88 (1984).
[51]A. N. Norris, "Back reflection of ultrasonic waves from a liquid–solid interface," J. Acoust. Soc. Am. **73**(2), 427–434 (1983).
[52]A. N. Norris, "The influence of beam type on the back reflection of ultrasonic beams from a liquid–solid interface," J. Acoust. Soc. Am. **76**(2), 629–631 (1984).
[53]A. M. Jessop, "Near-field pressure distributions to enhance sound transmission into multi-layer materials," Ph.D. thesis, Purdue University, West Lafayette, IN, 2013.
[54]Lord Rayleigh, "On waves propagated along the plane surface of an elastic solid," Proc. Lond. Math. Soc. **17**(1), 4–11 (1885).
[55]J. D. N. Cheeke, *Fundamentals and Applications of Ultrasonic Waves* (CRC, Boca Raton, FL, 2012), pp. 125–134.
[56]R. T. Beyer and S. V. Letcher, *Physical Ultrasonics* (Academic, New York, 1969), pp. 27–36.
[57]W. R. Chen, H. Liu, and R. E. Nordquist, "Mechanism of laser immunotherapy: Role of immunoadjuvant and selective photothermal laser–tissue interaction," in *Proceedings of the International Workshop on Photonics and Imaging in Biology and Medicine*, Wuhan, China (2002), pp. 82–89.
[58]M. G. Mack, K. Eichler, R. Straub, T. Lehnert, and T. J. Vogl, "MR-guided laser-induced thermotherapy of head and neck tumors," Med. Laser Appl. **19**(2), 91–97 (2004).
[59]A. Yousef Sajjadi, K. Mitra, and M. Grace, "Ablation of subsurface tumors using an ultra-short pulse laser," Opt. Lasers Eng. **49**(3), 451–456 (2011).
[60]Y. Peng, Z. Dai, H. A. Mansy, R. H. Sandler, R. A. Balk, and T. J. Royston, "Sound transmission in the chest under surface excitation: An experimental and computational study with diagnostic applications," Med. Biol. Eng. Comput. **52**(8), 695–706 (2014).
[61]T. H. El-Bialy, R. F. Elgazzar, E. E. Megahed, and T. J. Royston, "Effects of ultrasound modes on mandibular osteodistraction," J. Dental Res. **87**(10), 953–957 (2008).
[62]Ö. Erdogan and E. Esen, "Biological aspects and clinical importance of ultrasound therapy in bone healing," J. Ultrasound Med. **28**(6), 765–776 (2009).
[63]D. S. Moore, "Instrumentation for trace detection of high explosives," Rev. Sci. Instrum. **75**(8), 2499–2512 (2004).
[64]D. S. Moore, "Recent advances in trace explosives detection instrumentation," Sens. Imag. **8**(1), 9–38 (2007).
[65]H. Östmark, S. Wallin, and H. G. Ang, "Vapor pressure of explosives: A critical review," Propellants Explosives Pyrotechn. **37**(1), 12–23 (2012).
[66]D. C. Woods, J. K. Miller, and J. F. Rhoads, "On the thermomechanical response of HTPB composite beams under near-resonant base excitation," in *Proceedings of the ASME 2014 International Design Engineering Technical Conferences and Computers and Information in Engineering*

Conference, 26th Conference on Mechanical Vibration and Noise, Buffalo, NY (2014), No. DETC2014–34516, 11 pp.
[67]J. K. Miller, D. C. Woods, and J. F. Rhoads, "Thermal and mechanical response of particulate composite plates under inertial excitation," J. Appl. Phys. **116**(24), 244904 (2014).
[68]H. Cox, R. M. Zeskind, and M. M. Owen, "Robust adaptive beamforming," IEEE Trans. Acoust. Speech Signal Process. **35**(10), 1365–1376 (1987).
[69]B. D. Van Veen and K. M. Buckley, "Beamforming: A versatile approach to spatial filtering," IEEE ASSP Mag. **5**(2), 4–24 (1988).
[70]O. Kirkeby and P. A. Nelson, "Reproduction of plane wave sound fields," J. Acoust. Soc. Am. **94**(5), 2992–3000 (1993).
[71]O. Robin, A. Berry, and S. Moreau, "Experimental vibroacoustic testing of plane panels using synthesized random pressure fields," J. Acoust. Soc. Am. **135**(6), 3434–3445 (2014).